aerospace

MDPI

Article

Characterization of the Endwall Flow in a Low-Pressure Turbine Cascade Perturbed by Periodically Incoming Wakes, Part 2: Unsteady Blade Surface Measurements Using Pressure-Sensitive Paint

Tobias Schubert, Dragan Kožulović and Martin Bitter *

Institute of Jet Propulsion, University of the Bundeswehr Munich, Werner-Heisenberg-Weg 39, 85577 Neubiberg, Germany
* Correspondence: martin.bitter@unibw.de

Abstract: Unsteady pressure-sensitive paint (i-PSP) measurements were performed at a sampling rate of 30 kHz to investigate the near-endwall blade suction surface flow inside a low-pressure turbine cascade operating at engine-relevant high-speed and low-Re conditions. The investigation focuses on the interaction of periodically incoming bar wakes at 500 Hz with the secondary flow and the blade suction surface. The results build on extensive PIV measurements presented in the first part of this two-part publication, which captured the 'negative-jet-effect' of the wakes throughout the blade passage. The surface pressure distributions are combined with CFD to analyze the flow topology, such as the passage vortex separation line. By analyzing data from phase-locked PIV and PSP measurements, a wake-induced moving pressure gradient negative in space and positive in time is found, which is intensified in the secondary flow region by 33% with respect to midspan. Furthermore, two methods of frequency-filtering based on FFT and SPOD are compared and utilized to associate a pressure fluctuation peak around 678 Hz with separation bubble oscillation.

Keywords: pressure-sensitive paint; surface flow measurement; turbine cascade; unsteady flow

Citation: Schubert, T.; Kožulović, D.; Bitter, M. Characterization of the Endwall Flow in a Low-Pressure Turbine Cascade Perturbed by Periodically Incoming Wakes, Part 2: Unsteady Blade Surface Measurements Using Pressure-Sensitive Paint. *Aerospace* **2024**, *11*, 404. https://doi.org/10.3390/aerospace11050404

Academic Editor: Lin Chen

Received: 14 March 2024
Revised: 6 May 2024
Accepted: 7 May 2024
Published: 16 May 2024

1. Introduction

The establishment of high-lift blade designs in modern jet engines and the ongoing trend to reduce weight by lowering the solidity in low-pressure turbine (LPT) vanes has triggered a lot of research on endwall flow in recent years. The main motivation is the significant contribution to overall losses due to high pressure gradients in the blade passage and thus intensified endwall flow. In the case of low-aspect-ratio LPT blades, for which a larger range of the blade span is affected, the endwall losses are approximated to account for one third of the overall losses, see [1]. Based on a numerical parametric design study in LPT cascades, Coull [2] found that endwall losses can be decomposed into two major components: dissipation in the endwall boundary layer and induced losses by secondary flows, which scale with streamwise vorticity. According to Denton and Pullan [3], the secondary flow itself exhibits several sources of loss, such as flow interactions inside the blade passage and downstream mixing losses. Particularly, the interaction of the passage vortex and the blade suction surface, resulting in the counter rotating vortex, was found to have a strong contribution to the overall losses by Cui and Tucker [1] as well as Bear et al. [4]. The endwall flow development is also largely dependent on the inflow conditions. The effects of periodically incoming wakes were investigated in the T106A and T106Div turbine cascades using measurements and numerical simulations (CFD) by Ciorciari et al. [5,6]. Both approaches have shown an attenuation of the secondary flow. In contrast to the relatively small effects of incoming wakes, Volino et al. [7] found the influence of the inlet boundary layer to be much larger. Schubert and Niehuis [8] came to a similar conclusion when evaluating the turbine cascade exit flow; however, they found that

the endwall flow development inside the blade passage is significantly affected by both factors, but in different manners. The vast majority of research dealing with secondary flow investigations has been centered around probe-based measurements: mostly up- and downstream of the blade passage. More recently, some published works have diverged from this classic approach by incorporating more modern experimental methods. For example, Sinkwitz et al. [9] and Lopez et al. [10] utilized hot-film sensor arrays on the near-endwall suction surface, and Chemnitz and Niehuis [11] analyzed the potential of particle image velocimetry (PIV) in comparison to five-hole-probe (FHP) and constant temperature anemometry (CTA) measurements in turbine cascade exit flow.

Despite the vast research activity in recent years, the accurate prediction and reduction of endwall loss is expected to remain a challenge for many years to come [3]. Aimed at providing a further step in the continued understanding of endwall flow and its determining factors, an extensive research program funded by the Deutsche Forschungsgemeinschaft (DFG) was launched in 2018 by four German university institutes, see Engelmann et al. [12]. Within this conglomerate, the Institute of Jet Propulsion of the University of the Bundeswehr Munich covered low-pressure turbine aspects at high-speed flow conditions. This paper is based on the design work and first experimental and CFD results by Schubert et al. [8,13]. They used a particular turbine cascade design to investigate the effects of boundary layer conditions and periodically incoming wakes on the secondary flows and losses. The subsequent goal was to validate, complement, and specify the previous findings by conducting state-of-the-art optical measurements inside the blade passage, which poses a far greater challenge in terms of experimental setup. Thereby, the present work will demonstrate how the classic approach to secondary flow investigations can be extended and enhanced to form a more comprehensive picture. While the discussion of phase-locked PIV results was the focus of the first part [14] of this two-part publication, the second part will present unsteady pressure-sensitive paint (i-PSP) measurements on the blade suction surface.

In view of the high potential of the pressure-sensitive paint technique (PSP) demonstrated in the classical fields of experimental aerodynamics, its published application in turbomachinery research is rather low, compare, e.g., Liu et al. [15] or Lepicovsky and Bencic [16]. The standard works of Liu et al. [17] or Gregory et al. [18] reveal a large number of PSP applications covering nearly all branches of aerodynamics. The quality of the PSP results is impacted by various external factors, such as surface contamination, non-uniform surface temperatures, or limited optical access. This sensitivity often prevents the quantitative usage of the PSP technique in the area of rotating turbomachinery beyond simplified lab tests, as underlined, e.g., by Peng and Liu [19]. Nevertheless, Gao et al. [20] described the big potential of the turbomachinery research linked to (linear) blade cascades for the application and development of the PSP technique. As, e.g., Marks et al. [21], Gao et al. [22], and Dong et al. [23] have shown in steady inflow test cases, the knowledge of (unsteady) surface pressure enables a better understanding of complex aerodynamics like they may appear in a linear cascade, especially if the vortex interaction in the secondary flow regime is in focus. The author's motivation in choosing unsteady PSP to further resolve the surface dynamics of the wakes was raised by the experience of applying this experimental technique to answer turbomachinery-related research questions, compare Bitter et al. [24–26].

2. Methods

2.1. Test Case

The presented experiments were conducted using a linear cascade of the T106A low-pressure turbine profile. The key geometric and flow parameters are summarized in Table 1. The T106 cascade has a long research history, and the aerodynamic performance of the original design is well known under various operating conditions, see, e.g., Kampitsch et al. [27], Kirik and Niehuis [28], or Michelassi et al. [29]. However, the cascade used here is a redesign that was specifically developed for endwall flow measurements under

periodic inflow and high-speed conditions ($M_{2th} = 0.59$, $Re_{2th} = 2 \times 10^5$). The blade profile geometry remains unchanged, though. The main features of the current cascade are a sufficiently thick endwall boundary layer and the ability to perform variations in the boundary layer conditions on this endwall. The challenge regarding the endwall boundary layer stems from a gap between the wind tunnel and the cascade endwalls upstream of the blade passages. This gap, which is needed for the moving bar wake generator, enables a leakage flow driven by a negative pressure gradient. While the freestream flow is not affected, it can act as a boundary layer suction, leading to weak secondary flow. To counteract this problem, the current cascade features an integrated split flat plate at part-span that serves as a turbine endwall (marked in yellow in Figure 1). Using a modular composition of the aft plate, various measurement techniques can be implemented with manageable effort. The endwall boundary layer can be adjusted by misaligning the front plate with respect to the aft plate. During all measurements presented in this paper, the endwall boundary layer thickness was $\delta_{99} = 4.62$ mm with a shape factor of $H_{12} = 1.86$ at 45% Chord C upstream of the blade's leading edge (LE). A detailed description of the particular test case design and an investigation of the effects of endwall boundary layer variations on the secondary flow and loss production can be found in [8,13].

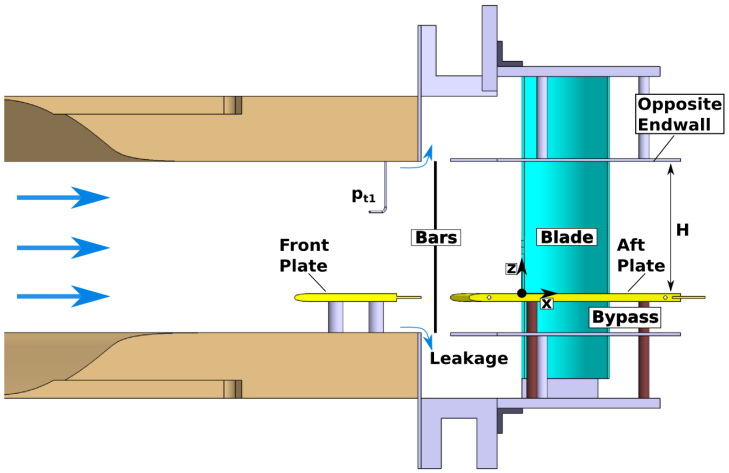

Figure 1. Illustration of the T106A test case featuring a split flat plate endwall (yellow) and moving bars upstream of the low-pressure turbine blades (cyan); adapted from Schubert et al. [8].

Table 1. T106A linear turbine cascade.

Geometric parameters:	
Chord length C	100 mm
Pitch-to-chord ratio P/C	0.799
Aspect ratio H/C	1.31
Flow conditions:	
Exit Mach number M_{2th}	0.59
Exit Reynolds number Re_{2th}	2×10^5
Design inflow angle β_1	127.7°
Design outflow angle β_2	26.8°
Turbulence intensity Tu_1	6.8%
Periodically unsteady inflow conditions:	
Strouhal number Sr	0.66
Flow coefficient ϕ	3.8

2.2. Numerical Setup

Numerical simulations were utilized during the cascade design (pre-test CFD) as well as to support the experimental results (validated post-test CFD) with time-resolved flow data, especially in areas of limited accessibility. The unsteady simulations were performed using the (U)RANS flow solver TRACE by DLR with the $k - \omega$ turbulence model by

Wilcox [30] and $\gamma Re_{\theta t}$ transition model by Langtry and Menter [31]. The computational domain covers a single blade pitch with periodic boundary conditions. It is divided into an upstream block group encompassing the front plate, a moving domain containing two bar pitches, and a downstream block group that encompasses the blade passage and aft plate. The leakage flow is simulated by additional outlet panels at the bar gap boundaries. The blade passage is discretized using an OCGH-topology and low-Reynolds wall treatment (non-dimensional wall distance $y+ \leq 1$), resulting in high boundary layer resolution. Sufficient spatial and temporal discretization is ensured by a sensitivity study, which leads to an overall number of nodes of approximately 8×10^6 and a blade o-grid with 354, 31, and 110 nodes in the i,j,k-directions, respectively. The CFL number is set to 150 in the unsteady simulations, and each moving domain period (two bar pitches) is resolved by 800 time steps. The flow conditions prescribed at the in- and outlet plane match the wind tunnel conditions in the experiment (M_{2th}, $Re_{2th} = f(T_{t1}, p_{t1}, p_3)$, and Tu_1). A detailed description of the computational approach can be found in [13].

The key flow characteristics inside the T106A blade passage are illustrated by means of CFD in Figure 2. Here, axial slices of the entropy generation rate and iso-surfaces of the Q-criterion (colored by streamwise vorticity indicating the sense of rotation) indicate loss production at midspan and the secondary flow region. In the 2D-flow region around midspan, the levels of loss production start off moderately in the predominately aft-loaded T106A. However, near the trailing edge (TE), strong adverse pressure gradients acting on the blade suction surface lead to the formation of a separation bubble. Under periodically unsteady inflow conditions, wake-induced transition periodically forces the suppression of the separation bubble. This unsteady effect is visible in the time-averaged flow in Figure 2 by a lack of alternating vorticity on the rear suction surface. Near the endwall, the formation of secondary flow as described e.g., by Sieverding [32] becomes apparent. When entering the blade passage, strong transverse pressure gradients caused by blade loading force the boundary layer fluid towards the suction surface. During this process, the flow is rolling up, is fed into the passage vortex and the merging horseshoe vortex pressure side leg, lifts off the endwall, and finally impinges on the blade suction surface. In addition to the resulting high losses, the secondary flow can be identified well by overturning close to the endwall and corresponding underturning at the upper edge of vortex interaction. In the case of unsteady inflow, the interaction of the wakes with the endwall boundary layer periodically delays the development of the passage vortex. This leads to the attenuation of the secondary flow further downstream and, hence, a reduction in the secondary losses. A more detailed analysis of the secondary vortex system and the associated loss generation mechanisms can be found in [13].

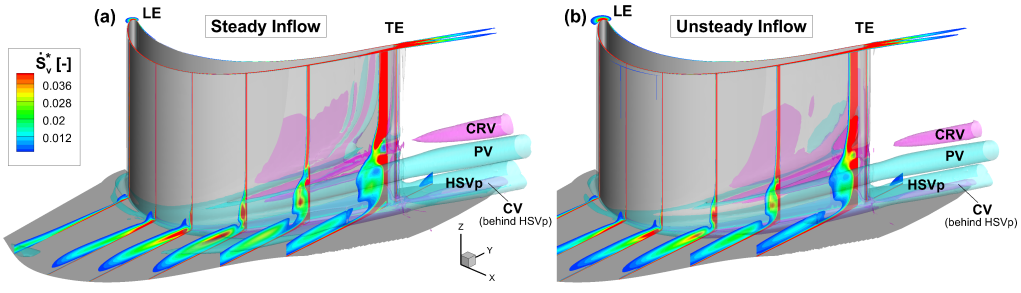

Figure 2. Simulated entropy generation rate ($\dot{S}_v^*$ non-dimensionalized) at several axial slices inside the T106A blade passage under steady (**a**) and periodically unsteady inflow conditions (**b**); adapted from Schubert et al. [13]; (HSVp—pressure side leg of horseshoe vortex; PV—passage vortex; CRV—counter-rotating vortex; CV—corner vortex; LE—leading edge; TE—trailing edge).

2.3. Experimental Setup

The experiments were conducted at the High-Speed Cascade Wind Tunnel (HGK) of the University of the Bundeswehr Munich, see Niehuis and Bitter [33]. The facility allows aerothermodynamic investigations of turbomachinery components at engine-relevant Mach

and Reynolds numbers, which can be varied independently with respective uncertainties of 0.17% and 0.28%. For this reason, the main components of the HGK are enclosed by a large plenum chamber with a 4 m diameter and a 12 m length. The absolute pressure in this plenum chamber can be evacuated down to 4 kPa or pressurized up to 1.2 MPa. The wide pressure range together with the large test section dimensions make it possible to perform aerodynamic investigations on relatively large test specimens, even for low operating Reynolds numbers. This mitigates the relative influence of probe-based measurement techniques on the flow field, especially at the high downstream Mach numbers typically encountered on a turbine cascade [34]. The HGK's test section can be equipped with a wake generator that produces periodically incoming wakes of up to around 500 Hz at the cascade inlet, see Acton and Fottner [35]. The periodically incoming wakes are generated by steel bars with a diameter of 2 mm, i.e., 111% of the T106A trailing edge diameter. The moving bar plane, which runs parallel to the blade passage inlet plane, is located 86% C upstream of the blade leading edge. The ratio of bars to blade count is two-to-one, i.e., $P_b/P = 0.5$, and the bar speed is $V_b = 20\,\mathrm{m/s}$, which leads to a bar passing period of 2 ms (500 Hz). Previous experimental and numerical studies of the T106A turbine cascade have shown that increased bar velocity (higher Strouhal number Sr and lower flow coefficient Φ) results in intensified effects on the secondary flow, see Ciorciari et al. [5]. However, within a reasonable range of unsteady inflow parameters, the observed trends remain unchanged. In addition to the mean velocity deficit, the bar wakes produce a turbulence intensity increase of around 20% in their core. Further detail including the downstream turbulence decay can be found in [36].

The focus of the present investigations is on the interaction between the blade profile flow, the periodically incoming wakes, and the secondary flow. For this purpose, intensity-based pressure-sensitive paint (PSP) was utilized to capture the pressure distribution on the suction surface. The PSP measurement principle is based on the detection of oxygen-dependent intensity of a fluorescence. For the fluorescence to be active, the luminophore, in the present case platinum(II)-tetrakis-fluorphenyl-porphyrin (PtTFPP), must be photo-chemically exited by near ultra-violet illumination. The oxygen dependency of the fluorescent intensity comes from a process known as oxygen quenching. Here, the excited molecules collide with ambient oxygen molecules and release their radiation energy until a relaxed state is reached. Therefore, the degression of fluorescence, and hence the intensity at a certain instance, can be linked to oxygen concentration, i.e., oxygen partial pressure. According to Henry's law, the static pressure of a gas mixture, in this case ambient air, is directly proportional to its oxygen partial pressure. This leads to the following polynomial known as the Stern–Volmer relation

$$\frac{I_{ref}}{I} = A(T) + B(T)\left(\frac{p}{p_{ref}}\right)^{n(T)}. \tag{1}$$

The coefficients $A(T)$, $B(T)$, and $n(T)$ exhibited a temperature dependency of $\approx$2.3%/K [26], but are also greatly affected by the composition of the active PSP layer. For the present experiments, the active PSP layer consisted of the luminophore and a porous, oxygen-permeable polymer-ceramic binder according to the formulation presented in Gregory et al. [18]. The coating was applied using a spray paint gun with a thickness of $\approx$20 µm and a mean roughness of $\approx$7 µm. Hence, a calibration specific to the measurement setup is required. In the present case, this was performed in two ways, both at constant $T_{t0} = 293\,\mathrm{K}$. The first method was a static pressure variation in the shutdown wind tunnel before testing. The second was an in situ calibration during testing using the static pressure taps on the blade surface. For the final results, the latter method was applied using a linear fit. As a illumination source, a wide UV-LED panel with a low-pass cut-off wavelength of 395 nm was mounted onto the wake generator (see Figure 3a,b). As seen in Figure 3c, a homogeneous illumination of the entire visible suction surface was achieved. The visible markers on the blade surface are an important feature for the data post-processing, which

allow a projection of the 2D image data onto a blade-fitted 3D grid. Due to the limited optical accessibility around the wake generator, the high-speed 4 Mpx sCMOS camera access (Phantom V2640) had to be realized using a mirror (see Figure 3a,b). Nevertheless, the full span of the highly curved suction surface was captured from $x/C_x = 0.64$ to the trailing edge. In order to enable an investigation of the periodic wake effects beyond the time average, the measurement setup was optimized for fast PSP response times. Ultimately, a 30 kHz sampling rate of a 896 × 432 px window was achieved for a measurement time of 8 s resulting in 240,000 intensity images. After each measurement, the wind tunnel and wake generator were shut down while keeping a constant chamber pressure p_c and inflow total temperature T_{t0} to record the reference intensity I_{ref} under static conditions for 0.5 s, i.e., 15,000 images. With each signal (I) and reference intensity (I_{ref}) measurement, 15,000 additional unilluminated images were recorded, averaged, and subtracted from the illuminated images in order to reduce background effects. An edge-preserving Gaussian bilateral image filter was applied, resulting in a final uniform data resolution of 1 mm.

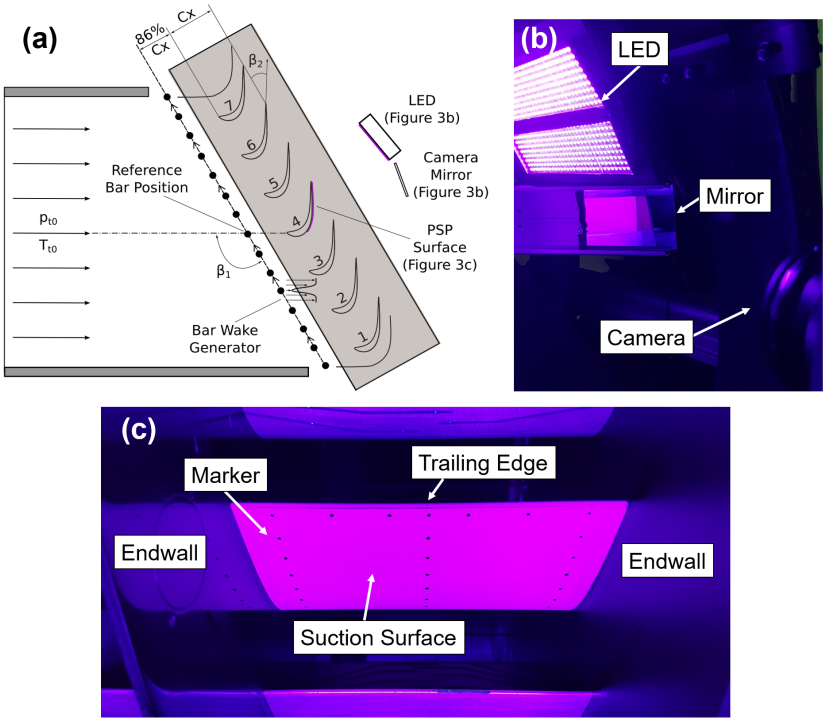

Figure 3. Experimental setup for unsteady pressure-sensitive paint (i-PSP) measurements in the T106A turbine cascade; (**a**) schematic of the cross-sectional side view; (**b**) camera access via a mirror and UV-light illumination; (**c**) camera view on the suction surface of the measurement blade (#4).

2.3.1. Validation

The PSP measurements were validated by a comparison to reference data from static pressure taps. Figure 4 illustrates the relative error after the in situ calibration with respect to each pressure tap $\Delta p_{rel} = (p_{PSP} - p_{PPT})/p_{PPT}$ and the resulting isentropic Mach number distribution at the midspan of the blade suction surface. The PSP data mostly exhibit slightly higher pressure values, i.e., a lower Mach number except for a slightly increased peak Mach number at $x/C_x = 0.67$ and a more distinct pressure plateau at the separation bubble near the trailing edge. However, the linear fit applied in the in situ calibration with a slope of 4.9 lead to an overall good match of the reference points with a R^2 value of 98.3% and RMS pressure deviations of 0.39% with a maximum of ±0.6%.

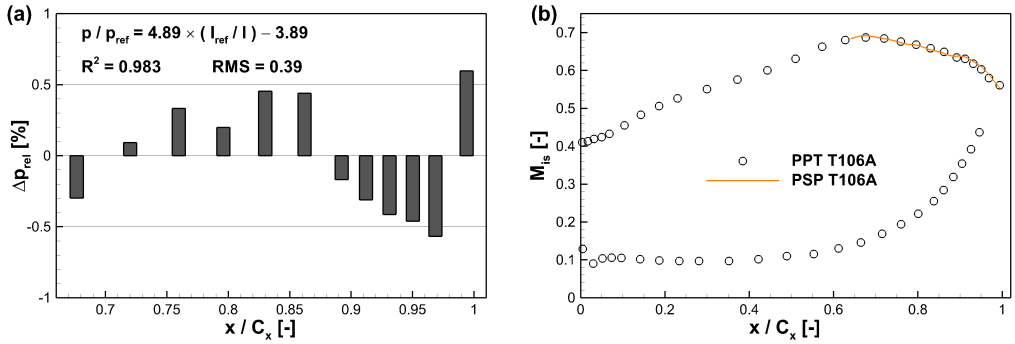

Figure 4. Comparison of the surface pressure measured with PSP, to static pressure taps at the midspan of the T106A turbine cascade under periodically unsteady inflow conditions; (**a**) relative pressure difference; (**b**) isentropic Mach number distribution.

2.3.2. Data Synchronization

In order to enable an investigation of the time-dependent effects of periodically incoming wakes, a phase-locking method according to Bitter and Niehuis [36] was applied to the PSP measurements as well as both PIV setups presented in part 1 [14]. Here, it is critical that the PSP sampling frequency and the dominant bar passing frequency (502 Hz) are decoupled so that the pitchwise bar positions are randomly distributed during the measurements. Synchronization is achieved in post-processing by establishing a correlation between the geometric bar position y_b and the temporal bar period t_{BP}. The first step is to define a reference bar position. In the experimental setup, a bar was aligned with the leading edge of the measurement blade by placing a steel ruler on top and leveling it (see Figure 5a). This reference bar position was then identified by measuring the current pitchwise distance $\Delta y_{b,ref}$ to the next trigger point of an optical sensor, which registers each passing bar (see Figure 5b,c). Finally, a timestamp τ was assigned for each measurement point by determining the relative time difference to the next bar trigger (see Figure 5d).

$$\frac{\tau}{t_{BP}} = \frac{t}{t_{BP}} - \frac{\Delta y_{b,ref}}{P_b}. \tag{2}$$

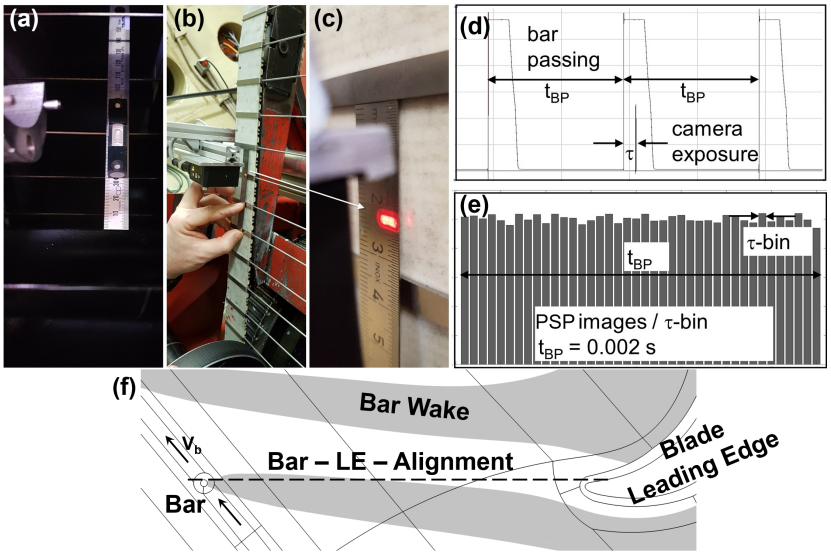

Figure 5. Phase-locking and synchronization method; (**a**–**c**) alignment of the spatial bar position with the temporal trigger signals of the bar counter; (**d**) assignment of a timestamp τ based on the rel. position in a bar passing period; (**e**) phase-averaging by binning in τ-bins of 25 µs; (**f**) application of the synchronization process to CFD by setting the reference bar position to $\tau = 0$.

In addition to data synchronization, binning the measured data according to their position within a bar passing period τ/t_{BP} was applied for phase-averaging. As seen in Figure 5e, this method led to a statistically uniform distribution of measurement points per τ-bin. This sorting method can be adjusted on demand. The more bins chosen, the higher the temporal resolution of the bar wake passing through the passage, but the lower the number of PSP images per bin for averaging the flow field. For the following discussions, 80 bins were chosen, including about 375 frames each. The synchronization process was also applied to the CFD data by determining the reference bar position and setting the correlating timestamp to zero (see Figure 5f).

3. Results

3.1. Time-Averaged Flow Fields

The ensemble, i.e., time-averaged static pressure fields on the rear section of the blade suction surface are illustrated in Figure 6. Only the lower half of the blade is displayed in cases under steady and periodically unsteady inflow conditions. Under steady inflow, the influence of the separation bubble on the rear suction surface is clearly visible. Downstream of the peak-Mach number line the positive pressure gradient (Mach number decrease) is interrupted by a pressure plateau, even a slight decrease, before further increasing to the exit pressure p_2. The outer limits of this region can be identified by the pressure inflection points $\frac{\partial^2 p}{\partial s^2} = 0$ (see 1a in Figure 6a). The downstream inflection points, where turbulent flow reattachment occurs, are accompanied by the high standard deviation of the pressure fluctuations (see 1b Figure 6b). This spanwise high-fluctuation band exhibits a upstream curvature in the transition to the secondary flow region. The position of the downstream inflection points is matched well in the numerical simulations in Figure 6c. However, the separation bubble with negative wall shear stress values due to local backflow is much narrower than in the measured PSP. Near the endwall, the secondary flows completely alter the blade pressure distribution by inducing lower static pressure. More precisely, the impingement of the horseshoe vortex pressure side leg (HSVp) effects the region closest to the endwall (see 2). The bent iso-lines above (see 3a) and the corresponding elevated fluctuations (see 3b) are a result of the surface flow interaction with the passage vortex (PV). The local streamlines on the upper side of the passage vortex point away from the blade surface, resulting in the PV separation line, which is not distinctly identifiable based on sole pressure data. With the support of CFD, it becomes apparent by a thin band of very low wall shear stress values (see 4 in Figure 6c). The resulting formation of the counter-rotating vortex (CRV) can be identified by a diagonal band of elevated shear stress just above the separation line (see 5a). Except for a slightly lower spanwise position, this correlates with a low-p'-band in the PSP data (see 5b). Also, the corner vortex forces local flow separation in the corner region between the endwall and the blade (see 6). Under periodically unsteady inflow conditions, the secondary flow is attenuated and, therefore, its imprint on the blade surface is less pronounced. Also, the passage vortex liftoff of the endwall is reduced (see 3c), leading to a larger 2D flow region around midspan. Here, an earlier wake-induced boundary layer transition results in a time-averaged suppression of the separation bubble. In the surface plots, this is apparent by the continuous pressure increase (see 1c), an upstream shift of a high-pressure fluctuation band (see 1d), and a lack of negative shear stress values due to local backflow (see 1e).

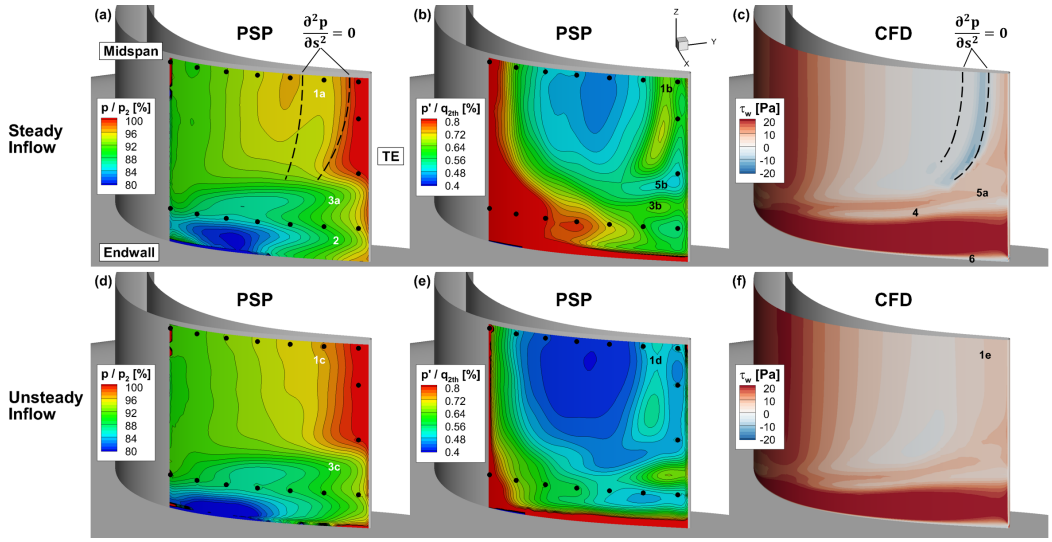

Figure 6. Measured static pressure distribution and supplemental CFD on the T106A suction surface under steady (**a**–**c**) and periodically unsteady (**d**–**f**) inflow conditions; (**a**,**d**) time-averaged pressure (PSP); (**b**,**e**) standard deviation of pressure fluctuations (PSP); (**c**,**f**) wall shear stress (CFD).

The frequency spectrum of the PSP measurement data is illustrated in Figure 7. As can be seen by the decreasing pressure amplitudes over the entire frequency range of 15 kHz, the measurement setup enabled a high-speed detection of small pressure fluctuations down to the single-digit Pascal range. The sporadic pressure peaks at very high frequencies can be attributed to aliasing effects. The dominant pressure signal of the bar wake generator at 502 Hz and its higher harmonics are clearly captured.

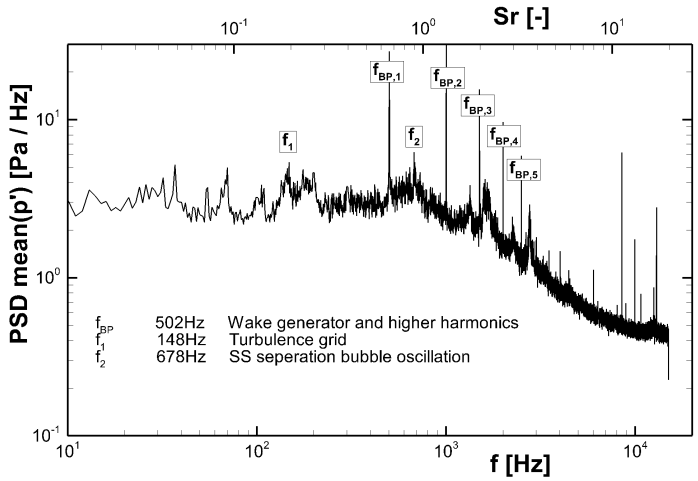

Figure 7. Power spectrum density of the mean pressure amplitudes (PSP) at midspan under periodically unsteady inflow conditions.

In order localize the wake-induced fluctuations amplitudes, two methods of frequency-based data filtering are compared in Figure 8. This was achieved by data conversion into the Fourier space (a) or by applying a spectral proper orthogonal decomposition averaged over 100 time steps (b,c). In the FFT-based data, the 2D flow at 502 Hz features spanwise (vertical) bands of high and low fluctuations. This pattern is similar to the alternating vorticity around midspan in the CFD results (see Figure 2a), and is associated to the wake effect on the highly loaded rear suction surface. The highly resolved distributions of pressure amplitudes and phase (not shown here) at distinct frequencies can also be used as input and validation data for frequency-based CFD methods, like the harmonic balance approach [37]. In the SPOD data at 502 Hz, two regions of positive and negative fluctuations

are present in the 2D flow. Both coincide with one of the consecutive high–low p'-patterns in the FFT data. In the secondary flow region, the fluctuations of the passage vortex are more clearly identifiable by a narrow streamwise band of fluctuation levels close to zero. This finding is in accordance to the phase-locked data discussed in the next chapter, where the periodic movement of the pressure iso-lines is limited to the streamwise direction. Just below this region is the fluctuation imprint of the HSV pressure side leg with negative amplitudes, indicating an opposite sense of fluctuation. Without prior knowledge of a source frequency, as in case of the wake generator, it can be difficult to associate pressure fluctuation peaks. In these cases, SPOD can be a valuable post-processing method to identify the fluctuation source. For example, at f_2 = 678 Hz, the amplitude distribution shows only negative signs and the dominant values are located near the trailing edge in the reattachment region. In the non-frequency-filtered data, this region is confined by the dominant secondary flow. In contrast, at f_2, it extends all the way to the endwall with little disturbance. Thus, this fluctuation peak can be associated to the separation bubble oscillation, which is confirmed by similar frequency ranges of comparable turbine blade profiles [36]. Some of the higher harmonics of the bubble oscillation, which is not distinctly at one frequency but rather a narrow range can be seen between the bar wake harmonics $f_{BP,2-5}$.

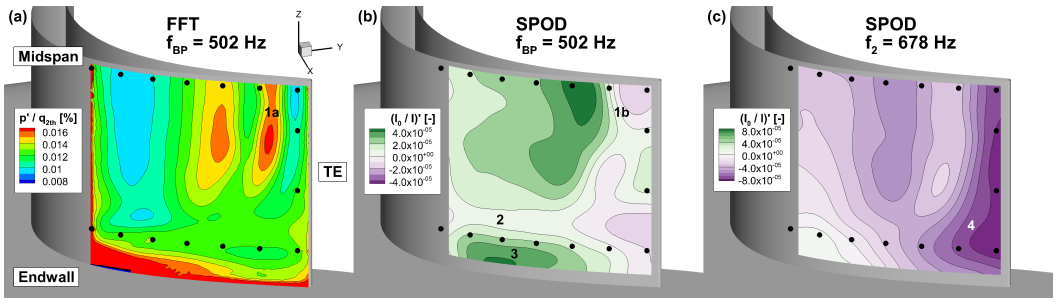

Figure 8. PSP measurements on the T106A suction surface stimulated by the first harmonic wake generator frequency of 502 Hz and the separation bubble osculation at 678 Hz; (**a**) FFT-based filtered pressure amplitudes; (**b**,**c**) first SPOD mode of the measured intensity ratios averaged over 100 time steps.

3.2. Phase-Locked Flow Fields

In order to further analyze the timely sequence leading to the presented time-averaged pressure fields, the phase-locked pressure fluctuations on the blade surface are illustrated at four time steps τ of one bar passing period t_{BP} in Figure 9. The normalized pressure fluctuations are given by $p'/q_{2th} = (\bar{p}(\tau) - \langle p \rangle)/q_{2th}$, where $\bar{p}(\tau)$ is the mean surface pressure of a τ-bin, $\langle p \rangle$ is the ensemble average over the entire time series, and q_{2th} is the theoretical dynamic pressure of the turbine exit flow. The indicated mean bar wake positions were determined by phase-locked PIV measurements in the blade-to-blade plane of the passage presented in part 1 [14]. Since the PIV data did not fully extend to the blade surface due to background reflections, the wake surface position had to be extrapolated (see Figure 10). The inherent uncertainties are mitigated by a validity check based on the measured imprint in the PSP surface data. At $\tau/t_{BP} = 0$, the bar wake impinges on the captured suction surface section and effects the majority of the flow with induced upstream higher pressure followed by downstream lower pressure (red to blue). In the secondary flow region closer to the endwall, the low pressure area extents to the trailing edge and the imprint of the passage vortex is apparent. This indicates an attenuation of the secondary flow even before the wake arrives.

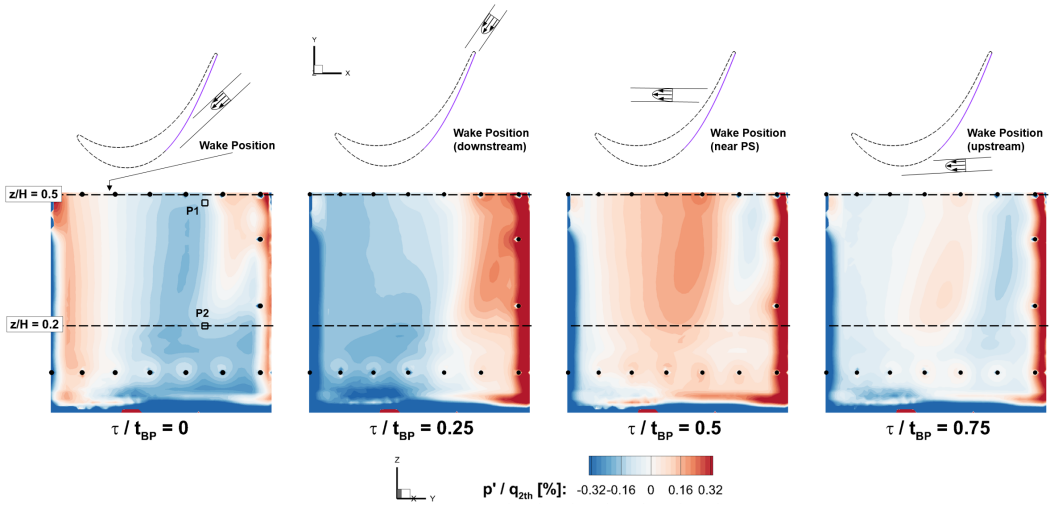

Figure 9. Phase-locked PSP pressure fluctuations measured on the T106A suction surface at four time steps of the bar passing period (the respective wake position is indicate above and the mean flow direction is from left to right).

Although the time-averaged PV liftoff is hereby reduced by the wakes, its phase-locked movement in spanwise direction is close to zero. Once the bar wake has traveled further downstream, only the high-pressure region associated to the wake is present close to the trailing edge at τ/t_{BP} = 0.25. In contrast to the previous time step, this effect extends over the entire blade span, albeit it is less intense near the endwall. Immediately after the wake has completely passed at around τ/t_{BP} = 0.35 , the pressure fluctuations across the captured suction surface section are close to zero. Halstead et al. describe this part of the bar period as a calming region in their time-space illustration at midspan [38]. The present results indicate that this description can be extended to the secondary flow region, where only minimal differences to the time-averaged flow field are present and the passage vortex imprint is not identifiable in p'-distribution (see Figure 11). At τ/t_{BP} = 0.5, the bar wake is located in the blade passage far from the suction surface (see Figure 10). This time step has the closest resemblance to the steady inflow case, which was measured separately as a reference. Most of the suctions surface exhibits elevated levels of pressure except for the 2D flow region close to the trailing edge. Here, a quick streamwise change from positive to negative pressure fluctuations indicates the reattachment of a separation bubble, which has formed in the absence of the bar wakes. The last time step in Figure 9 at τ/t_{BP} = 0.75 shows the upstream wake presence entering the field of view by a low pressure region on the left. However, the effects on the rear section are already establishing with a diminishing gradient in the 2D flow and near-endwall levels closer to the time-average.

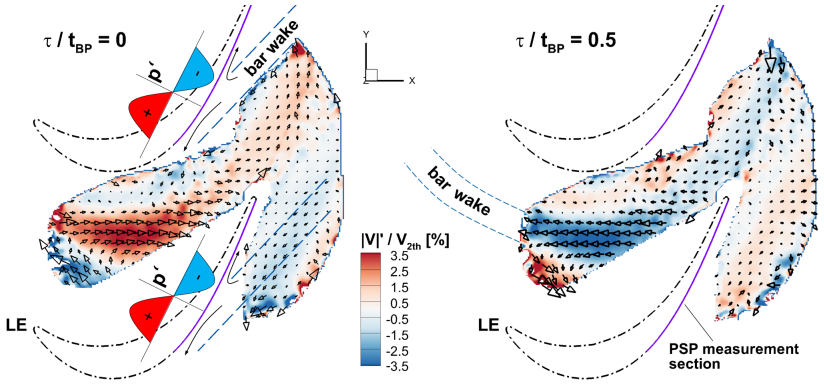

Figure 10. Phase-locked PIV measurements of the bar wake velocity deficit in the T106A turbine passage close to the endwall (z/H = 0.2) at two time steps and its effect on the blade surface pressure; adapted from part 1 [14].

A time-space correlation is used to further illustrate the phase-locked wake movement across the blade surface in Figure 11. The position of the wake, moving downstream in time, can be identified by a diagonal lane of relatively strong positive pressure gradients in time $\frac{\partial p}{\partial t} > 0$ (p' blue to red). The same effect appears as a negative spatial pressure gradient $\frac{\partial p}{\partial s} < 0$ (p' red to blue). The gradients connect a region of high pressure upstream of the wake and low pressure downstream of the wake. This sequence, also clearly visible in Figure 12, can be explained by the 'negative-jet-effect', where the velocity deficit of a bar wake forms a jet with negative flow direction relative to the free stream velocity. As illustrated in the sketch in Figure 10, the opposing pressure regions are a result of the relative streamline directions of the impinging negative jet. For example, downstream of the wake, i.e., before its passing, the negative jet streamline curvature points in the mean surface flow direction leading to an increased flow velocity and lower static surface pressure. The absolute amount of time Δt needed for the wake to move across the suction surface is mainly dependent on the Strouhal number. However, more relevant for the present investigation is the amount of time relative to one bar passing period $\Delta\tau/t_{BP}$, which is determined by the wake orientation inside the blade passage and thus the flow coefficient. Due to the relatively high flow coefficient in the present test case, the bowed wake has a very acute angle with respect to the rear suction surface (see Figure 10 and part 1 [14] for further detail). Therefore, the incline of the diagonal wake-lane in Figure 11 is quite flat. Moreover, the wake shape and orientation has an effect on the surface streamline curvature and, according to Hodson et al. [39], consequently, an effect on the amplitude of the up- and downstream pressure regions. This is the reason for the higher pressure gradients at $z/H = 0.2$ (see 1 in Figure 11c) than at midspan.

The part of the period where a separation bubble has formed in the absence of a wake can be identified by a local decrease in pressure (see 2a in Figure 11a) and a change from a high- to low-pressure fluctuation (p' red to blue), starting at ≈90% C_x at midspan (see 2b). This is not to be confused with the negative spatial pressure gradient induced by the wakes. In addition to the pressure gradient effect, the wake also induces a local turbulence increase, which strengthens the boundary layer robustness. This important factor cannot directly be captured by the sole surface pressure measurements and requires supplemental experimental or CFD data. In the present case, it leads to an earlier turbulent transition at midspan and a resulting periodic suppression of the separation bubble inside the wake-lanes. A difference between the two spanwise slices is apparent in the p' peak around $\tau/t_{BP} = 0.15$. The high amplitude at midspan is a result of the low reference pressure in the bubble reattachment region and, therefore, fades towards the endwall.

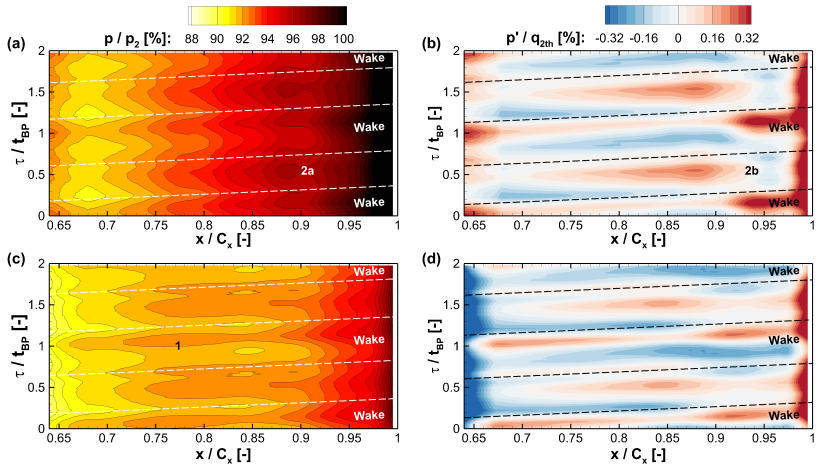

Figure 11. Time-space correlation of the measured static pressure distributions at midspan of the suction surface (**a**,**b**) and close to the endwall at $z/H = 0.2$ (**c**,**d**).

A comparison of the measured phase-locked pressure fluctuations with CFD results was performed in two locations, as illustrated in Figure 12. Position $P1$ is located in the 2D flow region around midspan, where the separation bubble appears ($x/C_x = 0.91$). $P2$ is located at the same streamwise position, but at $z/H = 0.2$, where the endwall effects become a factor (see Figure 9). The wake-induced upstream high-pressure and downstream low-pressure regions are apparent in both locations, with $p'/q_{2th} \approx \pm 0.16\%$ at $P1$ and $p'/q_{2th} \approx \pm 0.22\%$ at $P2$. The intensified wake effect near the endwall found in Figure 11 can be quantified here by a 33% increase of the 98 Pa/ms pressure gradient at midspan. Despite the different flow regimes at the two positions, the pressure fluctuations are in phase. This also holds true for the CFD data, however, there is a phase shift to the PSP signals of around 36°, i.e., $\Delta\tau/t_{BP} \approx 0.1$. While the pressure amplitudes and the basic periodic sequence can be reproduced in the numerical simulations, the predictions are not as accurate as in the case of the velocity field in the front part of the blade passage ($x/C_x = 0.3$). Here, a phase shift between 0° and 36° was presented in part 1 [14]. The main difference at $P1$ is an exaggeration of the low-pressure region before the wake passing, and thus a severe increase in the pressure gradient of 188%. This is caused by a well-known attenuation of the wake mixing process in RANS-based simulations, leading to more pronounced wakes further downstream. Adjusting the wake mixing to measured values would require a large increase in the modeled turbulent length scale, which, in return, would lead to unrealistic loss production levels. At $P2$ ($z/H = 0.2$), the wake-induced pressure gradient is well reproduced with a delta to the measurements of -7%, but during the wake absence, the pressure levels are elevated in the CFD. Overall, resolving the unsteady pressure fluctuations with single- to double-digit Pascal amplitudes is challenging for conventional simulation methods. Therefore, highly resolved surface pressure data measured with unsteady PSP, as presented here, has a high potential for CFD validation and provides a reference for improving numerical methods.

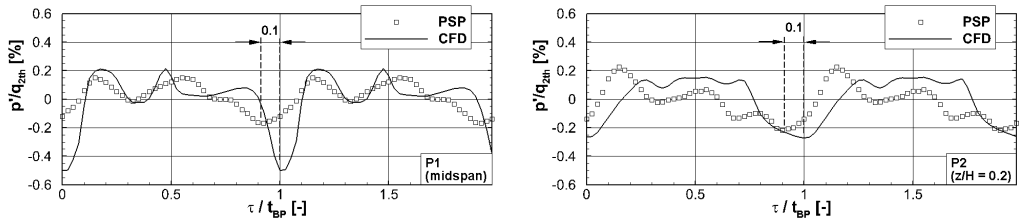

Figure 12. Comparison of CFD predictions of pressure fluctuations to phase-locked PSP measurements at position $P1$ (**left**) & $P2$ (**right**) marked in Figure 9.

4. Conclusions

An experimental campaign was conducted using the T106A linear turbine cascade with an additional part-span endwall under challenging measurement conditions with periodically incoming wakes with a frequency of 500 Hz. In previous investigations, the authors utilized a combination of probe-based measurements and CFD to identify an attenuation of the downstream secondary flow caused by wake interaction inside the blade passage. The primary goal of the experiments presented here was to validate, complement, and specify these findings.

The present work was split into two parts. The first part [14] dealt with resolving the unsteady passage flow field in a blade-to-blade plane with phase-locked PIV measurements. By tracing the wake throughout the passage, the 'negative-jet-effect' was clearly illustrated and the wake transport was related to the periodic secondary flow effects in an axial plane downstream of the passage. The goal of the second part was to resolve the static pressure field on the blade suction surface including the effects of the passing wakes. For this purpose, unsteady pressure-sensitive paint (i-PSP) was utilized at a 30 kHz sampling rate. The measurement area extended all the way to the endwall, enabling the identification of the secondary vortex imprints by low static pressure. In the 2D flow region around

midspan, the dominant pressure fluctuations were associated to the high blade loading at the rear suction surface. Here, the reattachment region with high p' is more apparent than the separation bubble itself. By combining phase-locked PIV and PSP data, the movement of the bar wakes across the suction surface was traced, which caused an upstream high-pressure and a downstream low-pressure region with around $\pm 0.2\%$ of the dynamic exit pressure (p'/q_{2th}). The resulting negative pressure gradient in space and positive gradient in time of 98 Pa/ms was increased in the secondary flow region by 33%. Furthermore, two methods of frequency-filtering based on FFT and SPOD were compared. By the example of separation bubble oscillation at 768 Hz, it was demonstrated how the latter can be utilized to associate a specific frequency range to its source flow phenomenon.

The PSP surface pressure data provided insight into the wake-perturbed secondary flow interaction and the resulting profile flow topology, but for some aspects, supplemental data are necessary. One example is the use of wall shear stress analysis to localize the passage vortex separation line and the resulting counter-rotating vortex. In the present case, RANS-based CFD proved to be a vital addition with sufficient accuracy despite a phase shift of around 36° and an exaggeration of the wake-induced pressure gradient at midspan. However, matching the unsteady single- to double-digit Pascal pressure fluctuations was more challenging than in the case of the passage flow field presented in part 1. Overall, it has been demonstrated that, particularly for secondary flow investigations under periodic inflow conditions, phase-locked optical measurements such as PIV and unsteady PSP provide a valuable addition to classic probe-based measurement approaches.

Author Contributions: Conceptualization, T.S.; Methodology, T.S. and M.B.; Software, T.S.; Validation, T.S.; Formal analysis, T.S.; Investigation, T.S.; Resources, D.K.; Data curation, T.S.; Writing—original draft, T.S.; Writing—review & editing, T.S. and M.B.; Visualization, T.S.; Supervision, D.K. and M.B.; Project administration, T.S. and M.B.; Funding acquisition, T.S. and M.B. All authors have read and agreed to the published version of the manuscript.

Funding: The numerical design as well as the experimental investigations presented in this paper were performed in the framework of the joint project PAK 948 "Flow near the endwall of turbomachinery blading" funded by Deutsche Forschungsgemeinschaft under the funding code Ma 4922/8-1.

Data Availability Statement: The raw data supporting the conclusions of this article will be made available by the authors on request.

Conflicts of Interest: The authors declare no conflicts of interest.

Nomenclature

Latin Symbols

C	chord length
H	channel height, i.e., blade span
M	Mach number
p	pressure
p'	pressure fluctuations
$\langle p \rangle$	ensemble-averaged pressure
P	pitch
q	dynamic pressure
R^2	coefficient of determination
Re	Reynolds number
s	blade surface coordinate
$\dot{S}_v^*$	non-dimensional entropy generation rate per unit volume, $\dot{S}_v \times (C \times T_{2,th})/(\rho_{2,th} \times V_{2,th})$
Sr	Strouhal number, $(V_b/P_b) \times (C/V_{x1})$
T	temperature
t	time
V	velocity
x, y, z	axial, pitchwise, and spanwise coordinate

Greek Symbols	
ϕ	flow coefficient, V_{x1}/V_b
τ	synchronized timestamp
Abbreviations	
CV	corner vortex
CRV	counter rotating vortex
EW	endwall
HSVp	horseshoe vortex pressure side leg
i-PSP	unsteady pressure-sensitive paint
LE	leading edge
MS	midspan
PIV	particle image velocimetry
PSP	pressure-sensitive paint
PV	passage vortex
TE	trailing edge
sCMOS	scientific complementary metal oxide semiconductor
Subscripts	
1	inflow condition
2	exit flow condition
b	bar
BP	bar passing
t	stagnation quantity
th	theoretical value after isentropic change of state

References

1. Cui, J.; Tucker, P.G. Numerical Study of Purge and Secondary Flows in a Low Pressure Turbine. In Proceedings of the ASME Turbo Expo 2016: Turbomachinery Technical Conference and Exposition, Seoul, Republic of Korea, 13–17 June 2016; ASME GT2016-56789.
2. Coull, J.D. Enwall Loss in Turbine Cascades. *J. Turbomach.* **2017**, *139*, 081004. [CrossRef]
3. Denton, J.; Pullan, G. A Numerical Investigation into the Sources of Endwall Loss in Axial Flow Turbines. In Proceedings of the ASME Turbo Expo 2012: Turbine Technical Conference and Exposition, Copenhagen, Denmark, 11–15 June 2012; ASME GT2012-69173.
4. Bear, P.; Wolff, M.; Gross, A.; Marks, C.R.; Sondergaard, R. Experimental Investigation of Total Pressure Loss Development in a Highly Loaded Low-Pressure Turbine Cascade. *J. Turbomach.* **2018**, *140*, 031003. [CrossRef]
5. Ciorciari, R.; Kirik, I.; Niehuis, R. Effects of Unsteady Wakes on Secondary Flows in the Linear T106 Turbine Cascade. *J. Turbomach.* **2014**, *136*, 091010. [CrossRef]
6. Ciorciari, R.; Schubert, T.; Niehuis, R. Numerical Investigation of Secondary Flow and Loss Development in a Low Pressure Tubrine Cascade with Divergent Endwalls. *Int. J. Turbomach. Propuls. Power* **2018**, *3*, 5. [CrossRef]
7. Volino, R. Effects on Endwall Boundary Layer Thickness and Blade Tip Geometry on Flow through High Pressure Turbine Passages. In Proceedings of the ASME Turbo Expo 2014: Turbine Technical Conference and Exposition, Düsseldorf, Germany, 16–20 June 2014; ASME GT2014-27013.
8. Schubert, T.; Chemnitz, S.; Niehuis, R. The Effects of Inlet Boundary Layer Condition and Periodically Incoming Wakes on Secondary Flow in a Low Pressure Turbine Cascade. *J. Turbomach.* **2021**, *143*, 041001. [CrossRef]
9. Sinkwitz, M.; Winhart, B.; Engelmann, D.; di Mare, F. Time-Resolved Measurements of the Unsteady Boundary Layer in an Annular Low-Pressure Turbine Configuration With Perturbed Inlet. *J. Turbomach.* **2021**, *144*, 011001. [CrossRef]
10. Lopes, G.; Simonassi, L.; Lavagnoli, S. Impact of Unsteady Wakes on the Secondary Flows of a High-Speed Low-Pressure Turbine Cascade. *Int. J. Turbomach. Propuls. Power* **2023**, *8*, 36. [CrossRef]
11. Chemnitz, S.; Niehuis, R. A Comparison of Turbulence Levels from Particle Image Velocimetry and Constant Temperature Anemometry Downstream of a Low-Pressure Turbine Cascade at High-Speed Flow Conditions. *J. Turbomach.* **2020**, *142*, 071008. [CrossRef]
12. Engelmann, D.; Sinkwitz, M.; di Mare, F.; Koppe, B.; Mailach, R.; Ventosa-Molina, J.; Fröhlich.; Schubert, T.; Niehuis, R. Near-Wall Flow in Turbomachinery Cascades—Results of a German Collaborative Project. *J. Turbomach. Propuls. Power* **2021**, *6*, 9. [CrossRef]
13. Schubert, T.; Niehuis, R. Numerical Investigation of Loss Development in a Low-Pressure Turbine Cascade with Unsteady Inflow and Varying Inlet Endwall Boundary Layer. In Proceedings of the ASME Turbo Expo 2021: Turbomachinery Technical Conference and Exposition, Virtual, 7–11 June 2021; ASME GT2021-59696.
14. Schubert, T.; Kožulović, D.; Bitter, M. Characterization of the Endwall Flow in a Low-Pressure Turbine Cascade Perturbed by Periodically Incoming Wakes, Part 1: Flow Field Investigations with Phase-Locked Particle Image Velocimetry. *Aerospace* 2024, *11*, 403. [CrossRef]

15. Liu, T.; Torgerson, S.; Sullivan, J.; Johnston, R.; Fleeter, S. Rotor Blade Pressure Measurement in a High Speed Axial Compressor Using Pressure and Temperature Sensitive Paints. In Proceedings of the 35th Aerospace Sciences Meeting and Exhibit, Reno, NV, USA, 6–9 January 1997.
16. Lepicovsky, J.; Bencic, T. Use of Pressure-Sensitive Paint for Diagnostics in Turbomachinery Flows with Shocks. *Exp. Fluids* **2002**, *33*, 531–538. [CrossRef]
17. Liu, T.; Sullivan, J.; Asai, K.; Klein, C.; Egami, Y. *Pressure and Temperature Sensitive Paints*, 2nd ed.; Experimental Fluid Mechanics; Springer: Berlin, Germany, 2021.
18. Gregory, J.; Sakaue, H.; Liu, T.; Sullivan, J. Fast Pressure-Pensitive Paint for Flow and Acoustic Diagnostics. *Ann. Rev. Fluid Mech.* **2014**, *46*, 303–330. [CrossRef]
19. Peng, D.; Liu, Y. Fast Pressure-Sensitive Paint for Understanding Complex Flows: From Regular to Harsh Environments. *Exp. Fluids* **2020**, *61*, 1–22.
20. Gao, L.; Gao, J.; Wang, H.; Liu, B.; Zhou, Q. Application of PSP Technique to Pressure Measurement on Cascade Surface. *J. Eng. Thermophys.* **2011**, *32*, 411–414.
21. Marks, C.; Fletcher, N.; Sondergaard, R. Vortex Unsteadiness in the Endwall Region of a High-Lift Low-Pressure Turbine Passage. *J. Turbomach.* **2022**, *145*, 011012. [CrossRef]
22. Gao, L.; Yang, G.; Gao, T.; Li, R.; Hu, X. Experimental Investigation of a Linear Cascade with Large Solidity Using Pressure Sensitive Paint and Dual-Camera System. *J. Therm. Sci.* **2021**, *30*, 682–695. [CrossRef]
23. Dong, Z.; Gu, F.; Chen, R.; Yang, J.; Zhou, W.; Liu, Y.; Peng, D. Three-Dimensional Pressure Field Measurement on Turbine Guide Vanes Using a Dynamic Distortion Correction Endoscopic Pressure-Sensitive Paint Technique. *Exp. Fluids* **2023**, *64*, 97. [CrossRef]
24. Bitter, M.; Wartzek, F.; Übelacker, S.; Schiffer, H.P.; Kähler, C. Investigation of a Distorted Transonic Compressor Flow using Two-Component Pressure-Sensitive Paint. In Proceedings of the 10th Pacific Symposium on Flow Visualization and Image Processing (PSFVIP 10), Naples, Italy, 15–18 June 2015.
25. Bitter, M.; Kurz, J.; Kähler, C.; Niehuis, R. Investigations of a Low-Pressure Turbine Blade by Means of Simultaneous Optical Velocity and Pressure Measurements. In Proceedings of the 18th International Symposium on Applications of Laser Techniques to Fluid Mechanics, Lisbon, Portugal, 4–7 July 2016.
26. Bitter, M.; Stotz, S.; Niehuis, R. On High-Resolution Pressure Amplitude and Phase Measurements Comparing Fast-Response Pressure Transducers and Unsteady Pressure-Sensitive Paint. *J. Turbomach.* **2021**, *143*, 031012. [CrossRef]
27. Kampitsch, M.; Stadtmüller, P.; Fottner, L. Investigations of Wake-Induced Transition on the LPT Cascades T106A-EIZ and T106D-EIZ. In Proceedings of the ERCOFTAC Workshop, La Clusaz, France, 19–23 March 2000.
28. Kirik, I.; Niehuis, R. Comparing the Effect of Unsteady Wakes on Parallel and Divergent Endwalls in a LP Turbine Cascade. In Proceedings of the 11th International Gas Turbine Congress, Tokyo, Japan, 15–20 November 2015; IGTC2015-137.
29. Michelassi, V.; Chen, L.; Pichler, R.; Sandberg, R.D. Compressible Direct Numerical Simulation of Low-Pressure Turbines—Part II: Effect of Inflow Disturbances. *J. Turbomach.* **2015**, *137*, 071005. [CrossRef]
30. Wilcox, D.C. *Turbulence Modeling for CFD*, 4th ed.; DCW Industries: La Canada, CA, USA, 2004.
31. Langtry, R.B.; Menter, F.R. Transition Modeling for General CFD Applications in Aeronautics. In Proceedings of the 43rd AIAA Aerospace Sciences Meeting and Exhibit, Reno, NV, USA, 10–13 January 2005; AIAA Paper 2005-522.
32. Sieverding, C. Recent Progress in the Understanding of Basic Aspects of Secondary Flows in Turbine Blade Passages. *ASME J. Eng. Gas Turbines Power.* **1985**, *107*, 248–257. [CrossRef]
33. Niehuis, R.; Bitter, M. The High-Speed Cascade Wind Tunnel at the Bundeswehr University Munich after a Major Revision and Upgrade. *Int. J. Turbomach. Propuls. Power* **2021**, *6*, 41. [CrossRef]
34. Börner, M.; Bitter, M.; Niehuis, R. On the Challenge of Five-Hole-Probe Measurements at High Subsonic Mach Numbers in the Wake of Transonic Turbine Cascades. *J. Global Power Propuls. Soc.* **2018**, *2*, 453–464. [CrossRef]
35. Acton, P.; Fottner, L. The Generation of Instationary Flow Conditions in the High-Speed Cascade Wind Tunnel of the German Armed Forces University Munich. In Proceedings of the 13th Symposium on Measuring Techniques, Zurich, Switzerland, 5–6 September 1996.
36. Bitter, M.; Niehuis, R. Effects of Periodic Inflow Turbulence on the Statistics in the Wake of a Linear LPT Cascade at Jet-Engine relevant Test Conditions. In Proceedings of the 13th International Symposium on Particle Image Velocimetry, Munich, Germany, 22–24 July 2019.
37. Frey, C.; Ashcroft, G.; Kersken, H.P.; Voigt, C. A Harmonic Balance Technique for Multistage Turbomachinery Applications. In Proceedings of the ASME Turbo Expo 2014: Turbine Technical Conference and Exposition, Düsseldorf, Germany, 16–20 June 2014; ASME GT2014-25230.
38. Halstead, D.E.; Wisler, D.C.; Okiishi, T.H.; Walker, G.J.; Hodson, H.P.; Shin, H. Boundary Layer Development in Axial Compressors and Turbines: Part 3 of 4–LP Turbines. *J. Turbomach.* **1997**, *119*, 225–237. [CrossRef]
39. Hodson, H.P.; Hynes, T.P.; Greitzer, E.M.; Tan, C.S. A Physical Interpretation of Stagnation Pressure and Enthalpy Changes in Unsteady Flow. *J. Turbomach.* **2012**, *134*, 060902. [CrossRef]